




Cite this: *J. Mater. Chem. B*, 2025, 13, 4471

Enhanced catalytic efficiency of nanozymes with a V-structured chip for microfluidic biosensing of *S. typhimurium*†

Ming-Yue Gao, Meng Wang, Yong-Tao Wang and Zhi-Ling Zhang *

Nanozymes, nanomaterials with enzyme-like characteristics which exhibit lower cost, easier synthesis and functionalization, and better stability compared with natural enzymes, have been widely developed for biosensing, disease therapy and environmental governance. However, the lack of catalytic efficiency of nanozymes compared to natural enzymes makes it difficult for them to completely replace natural enzymes to achieve higher sensitivity and lower detection limits in biosensing. Herein, magnetism-controlled technology was used to form a nanozyme array consisting of stacked $\text{Fe}_3\text{O}_4/\text{Au}$ NPs at the bottom of the microchannel as a spatially confined microreactor for the catalytic reaction. By enhancing the mass transfer process of the substrate towards nanozymes mediated by the corresponding V-structure, a higher local concentration of the substrate and more efficient utilization of active sites of nanozymes were achieved to increase the catalytic efficiency ($k_{\text{cat}}/K_{\text{M}}$) of the nanozyme array consisting of $\text{Fe}_3\text{O}_4/\text{Au}$ NPs by 95.2%, which was two orders of magnitude higher than that of the open reactor. Based on this, a colorimetric method on an integrated microfluidic platform was proposed for sensitive biosensing of *Salmonella typhimurium*. The entire detection could be completed within 30 minutes, yielding a linear range from 10^2 to 10^7 CFU mL^{-1} and a detection limit as low as 5.6 CFU mL^{-1} .

Received 24th January 2025,
Accepted 9th March 2025

DOI: 10.1039/d5tb00172b

rsc.li/materials-b

1. Introduction

Nanozymes, nanomaterials with enzyme-like characteristics which exhibit lower cost, easier synthesis and modification, better stability, and comparable catalytic activity toward specific substrates in comparison with natural enzymes, have been considered as the next generation of artificial enzymes.¹ Moreover, the unique physicochemical properties of nanozymes including magnetic, acoustic and optical properties further broaden their application in biosensing, disease therapy, anti-bacterial application and environmental governance.^{2,3} Benefiting from the capacity of signal amplification and signal conversion into measurable signals such as colorimetric,^{4–6} electrochemical,⁷ thermal⁸ and fluorescence⁹ signals, nanozymes have been widely applied for the bioanalysis of small molecules, proteins, nucleic acids, cells, bacteria, viruses, and so on.¹⁰ However, the catalytic efficiency of most nanozymes is still lower than that of natural enzymes due to structural differences, which restrict them from obtaining higher sensitivity and lower detection limits in biosensing.^{11,12}

To address this issue, many efforts have been made for modulating the composition and structure of nanozymes to obtain higher catalytic activity including size and morphology control,^{13,14} heteroatom doping,¹⁵ surface modification^{16–18} and mimicking the active sites of natural enzymes.^{19,20} In addition, controlling the catalytic environment of the solution such as the pH value,²¹ ions,²² and external energy fields^{23,24} can also enhance the catalytic activity of nanozymes. Through the above methods, the substrate adsorption or electron transfer process during the catalysis of specific substrates by nanozymes can be significantly improved, thus achieving higher catalytic efficiency. However, the mass transfer process of substrates to nanozymes, as the most fundamental step, should also be taken into consideration. For instance, the mass transfer resistance in the solution can be reduced by incorporating suitable surfactants into the catalytic system.²⁵

Over decades, flow catalysis including continuous flow catalysis, circulating flow catalysis, and swirl flow catalysis have been proven to improve the catalytic performance of catalysts by reducing the diffusion limitation and concentration non-uniformity of reactants transferring to the surface of the catalysts, thus exhibiting faster reaction kinetics.²⁶ Microreactors with extremely small dimensions and a large specific surface area²⁷ which can provide more accurate reaction conditions, higher mass transfer efficiency and heat transfer efficiency have been widely used to achieve rapid and efficient continuous flow

College of Chemistry and Molecular Sciences, Wuhan University, Wuhan, 430072, People's Republic of China. E-mail: zlzhang@whu.edu.cn

† Electronic supplementary information (ESI) available. See DOI: <https://doi.org/10.1039/d5tb00172b>



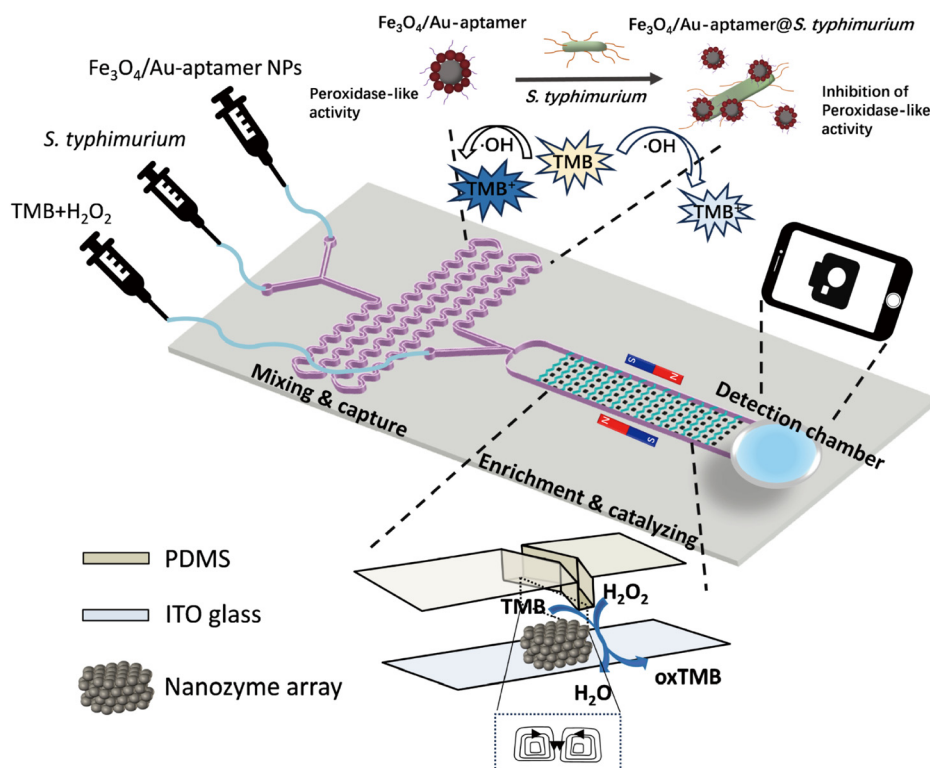
catalysis in the chemical-pharmaceutical industry,^{28,29} organic synthesis,³⁰ electrocatalysis,^{26,31} and pollutant treatment.^{32,33}

Recently, the microfluidic chip has been applied to provide confined space in nanzyme reactions for signal amplification. By maintaining the increased local concentration gradient and efficient mass transfer of the intermediate, the catalytic reaction efficiency of the cascade nanzyme system of the spatially confined continuous-flow microreactor can be improved by orders of magnitude compared with that of the open reactor, obtaining a significantly lower detection limit.^{34,35} In our previous work, a corresponding V-target lattice structure was constructed to enhance the binding process between oligonucleotide libraries and the target-coated arrays through fluid recycling in microfluidic-SELEX.³⁶ It is noteworthy that the remarkable enhancement of mass transfer by the corresponding V-structure can also be applied to improve the reaction efficiency between the substrates and nanozymes to achieve sensitive biosensing.

In this work, $\text{Fe}_3\text{O}_4/\text{Au}$ nanoparticles ($\text{Fe}_3\text{O}_4/\text{Au}$ NPs) with peroxidase-like activity were synthesized *via* an *in situ* reduction method. A nanzyme array consisting of stacked $\text{Fe}_3\text{O}_4/\text{Au}$ NPs was formed at the bottom of the channel right below the corresponding V-shaped structure under the attraction of the gradient magnetic field between the nickel lattices, which was induced by a pair of permanent magnets. The simulation results obtained using COMSOL Multiphysics software showed that the V-structure could form a higher local concentration of substrate inside the array, where restricted diffusion distance between the substrates and nanozymes could improve the catalytic reaction rate. In addition, the uniform distribution

of the substrate solution around the array enabled the active sites on the surface of the nanozymes to be more fully utilized. Thus, the catalytic efficiency ($k_{\text{cat}}/K_{\text{M}}$) of the $\text{Fe}_3\text{O}_4/\text{Au}$ NPs in the microfluidic chip increased by 95.2% in the presence of the optimized V-structure, which was two orders of magnitude higher than that of the open reactor according to the Michaelis-Menten equation. Furthermore, this strategy was applied for signal amplification in a $\text{Fe}_3\text{O}_4/\text{Au}$ nanzyme-assisted colorimetric method for foodborne pathogen biosensing on an integrated microfluidic platform. In addition, the microfluidic chip was magnetism-controlled, enabling rapid separation of the products and nanozymes, further simplifying the detection process.

As can be seen in Scheme 1, the microfluidic chip integrated the entire detection process including incubation, enrichment and catalyzing, and signal readout. The aptamer coated $\text{Fe}_3\text{O}_4/\text{Au}$ nanoparticles ($\text{Fe}_3\text{O}_4/\text{Au}$ -aptamer NPs) and *Salmonella typhimurium* (*S. typhimurium*) were firstly injected into the microfluidic chip simultaneously to form the $\text{Fe}_3\text{O}_4/\text{Au}$ -aptamer@*S. typhimurium* complexes, mixed by the serpentine microchannel. The peroxidase-like activity of the $\text{Fe}_3\text{O}_4/\text{Au}$ -aptamer NPs can be inhibited with the addition of the target bacteria,³⁷ which formed a blocking layer on the surface and caused the increasing inaccessibility between the substrates and catalytic active sites. After the mixing zone, the magnetic $\text{Fe}_3\text{O}_4/\text{Au}$ -aptamer@*S. typhimurium* complexes array was formed below the V-shaped structure correspondingly. Finally, the chromogenic solution (pH = 4 HAC-NaAc buffer containing TMB and H_2O_2) was forcibly transferred to the surface and interior of the corresponding V-nanzyme array to initiate efficient catalytic reaction



Scheme 1 Schematic of this microfluidic platform for *S. typhimurium* biosensing.



with the reciprocation of the precise syringe pump. The amplified blue color signal from oxTMB gathered in the detection chamber which indicated the concentration of *S. typhimurium* was read by the smartphone and further analyzed by ImageJ software. Under optimal experimental conditions, the proposed Fe₃O₄/Au nanozyme-assisted integrated microfluidic system can detect *S. typhimurium* from 10² to 10⁷ CFU mL⁻¹ in 30 min with a detection limit of 5.6 CFU mL⁻¹.

2. Materials and methods

2.1. Materials

3,3',5,5'-Tetramethylbenzidine (TMB) and iron(III) chloride hexahydrate (FeCl₃·6H₂O, 98%) was purchased from Shanghai Aladdin Reagents Co., Ltd (Shanghai, China). Iron(II) chloride tetrahydrate (FeCl₂·4H₂O, 99%), ammonium hydroxide (NH₃·H₂O), chloroauric acid tetrahydrate (HAuCl₄·4H₂O), hexadecyltrimethylammonium bromide (CTAB), ethylenediaminetetraacetic acid disodium salt dihydrate (Na₂EDTA·2H₂O), hydrogen peroxide (H₂O₂, 30%), sodium hydroxide (NaOH), sodium acetate (NaAc), acetic acid (HAc), sulfuric acid (H₂SO₄) and dimethyl sulfoxide (DMSO) used to pre-dissolve TMB were all obtained from Sinopharm Chemical Reagent Co., Ltd (Shanghai, China). Hydroxylammonium chloride (NH₂OH·HCl) was purchased from Chengdu Kelong Chemical Co., Ltd (Chengdu, China). Tris (2-carboxyethyl) phosphine hydrochloride (TCEP) was purchased from Shanghai Macklin Biochemical Co., Ltd (Shanghai, China). The water used in all experiments was 18.2 MΩ cm ultrapure water. The DNA aptamer of *S. typhimurium* used in a previously reported work³⁸ (5'-SH-ATAGGAGTCACGACGACCA GAAAGTAATGCCCGGTAGTTATTCAAAGATGAGTAGGAAAAGATA TGTGCGTCTACCTCTTGACTAAT-3') was synthesized and purified by Sangon Biotechnology Co., Ltd (Shanghai, China).

2.2. Apparatus

Transmission electron microscopy (TEM) characterization and energy dispersive spectrum (EDS) mapping were performed on a JEM-2100F transmission electron microscope (JEOL, Japan). X-ray diffraction (XRD) was conducted on a SmartLab 9kW X-ray diffractometer (Rigaku, Japan). The UV-vis absorbance and spectra were recorded by a UV-2550 spectrophotometer (Shimadzu, Japan). The steady-state kinetics were studied on a microplate reader (Synergy H1, BioTek, America). Zeta potential and hydrated particle size were tested on a dynamic light scattering (DLS) system (Zetasizer Nano-ZS, Malvern, England). Fourier transform infrared (FTIR) analysis was carried out on a Nicolet-6700 FTIR spectrometer (Thermo Fisher Scientific, America). The images of the detection chamber in the microfluidic chip were taken with an iPhone12 (Apple, America).

2.3. Bacterial culture

The bacterial strains used in this work were *S. typhimurium* (ATCC 14028), *P. aeruginosa* (ATCC 9027), *L. monocytogenes* (ATCC 19111), *E. coli* O157:H7 (CCTCC AB 91112), and *S. aureus* (CCTCC AB 91093). The colonies were resuscitated on Luria-Bertani

(LB) agar plates to obtain respective single colonies which were further inoculated and cultured in LB medium for 16–24 h at 37 °C with shaking at 180 rpm. The concentration of each kind of bacteria was measured using the standard colony counting method. After that, the bacteria were inactivated in 1% (v/v) formaldehyde solution overnight at 4 °C for further use. The inactivated bacteria were washed three times (5000 rpm, 5 min) and diluted 10-fold serially with sterile phosphate-buffered saline (PBS, 0.01 M, pH 7.4) to obtain the bacteria suspensions at the desired concentration.

2.4. Synthesis of Fe₃O₄/Au NPs

The Fe₃O₄ NPs were prepared by a co-precipitating method. FeCl₃·6H₂O and FeCl₂·4H₂O (1 : 2) were pre-dissolved in 0.01 M HCl under vigorous agitation at 40 °C for 10 min until the solids were fully dissolved. Then, the solution was gradually heated to 70 °C, while approximately 12 mL of NH₃·H₂O was added dropwise until pH = 10. Later, the mixture was stirred at 500 rpm for 30 min under nitrogen protection. After placed for another 30 min, the products were collected magnetically. Finally, the products were washed three times with first ultrapure water and then anhydrous ethanol respectively. After dried overnight in a vacuum oven at 50 °C, the Fe₃O₄ NPs were ground with an agate mortar and stored at 4 °C.

The prepared Fe₃O₄ NPs were further decorated with gold nanoparticles (Au NPs) according to previously reported work^{37,39} with minor modification. Briefly, 0.02 g of Fe₃O₄ NPs were uniformly dispersed in 5 mL of ultrapure water ultrasonically. Then, 0.5 g of Na₂EDTA·2H₂O dissolved in 5 mL of 1 M NaOH solution was added and stirred at 400 rpm for 5 min. The supernatant was separated from the solution by a permanent magnet. Then, 7 mL of 0.1 M CTAB, 3 mL of 1% HAuCl₄ and 600 μL of 1 M NaOH were added in turn. The solution was heated to 60 °C and stirred at 400 rpm for 5 min. Finally, 150 mg of NH₂OH·HCl was added as a reducing agent and the mixture was stirred for another 5 min. The dark purple products were collected by magnetic separation after the products were left to stand for 24 h at room temperature. The products were washed three times with first ultrapure water and then anhydrous ethanol respectively. The Fe₃O₄/Au NPs were dried overnight in a vacuum oven at 50 °C and stored at 4 °C. Glass flasks used in the synthesis process above were immersed in aqua regia solution overnight before use.

2.5. The design and fabrication of the microfluidic chip

The serpentine incubation channel (22 mm × 24 mm) has two sets of inlets and an outlet connected to an enrichment and catalyzing zone. The height of the channel was about 165 μm. The enrichment and catalyzing zone (15 mm × 0.8 mm) were designed along with a detection chamber (Φ = 5 mm). The magnetic field was induced by two opposite permanent magnets (15 × 5 × 3 mm). The integrated microfluidic chip was fabricated by standard photolithography. The microchannel with the corresponding V-shaped superstructure and the indium tin oxide (ITO) substrate with the staggered nickel pattern structure were fabricated according to our previous work.³⁶ For further use, the serpentine microchannel and the V-shaped superstructure



microchannel were bonded with glass and encapsulated ITO substrate, respectively, after plasma cleaning for 2 min.

To optimize the detailed parameters of the V-shaped superstructure, the pressure on the upper surface of the array exerted by fluid cycling was simulated by COMSOL Multiphysics. The inlet velocity was set to 0.00167 m s^{-1} and the outlet static pressure was set to 0 Pa. The boundary condition of the wall was set as the no-slip condition. By solving the steady-state Navier–Stokes equations, the average upper surface pressure of the array corresponding to the V-structure with alternative rate and different angles was simulated, respectively. Improvement rate was obtained according to $(P - P_0)/P_0$, where P and P_0 represent the average upper surface pressure in the presence and absence of V-structure. For further determining the arm width and the height of the V-structure as well as the overall height of the microchannel, since these parameters would affect the volume of the channel model and lead to a lack of regularity in the pressure simulation results, a single lattice unit model consisting of stacked microspheres was adopted in place of the solid array model. The volume of fluid entering the interior of the lattice unit through the front and upper surface is considered as the reaction volume V_{total} :

$$V_{\text{total}} = \left(\left| \iint_{S_1} \nu_x dS \right| + \left| \iint_{S_2} \nu_z dS \right| \right) \times \Delta t$$

where S_1 and S_2 refer to the front and top surface of the lattice unit, while ν_x and ν_z are the velocity components in the x -direction and z -direction. The dS represents an infinitesimal area element. The time Δt for the fluid to flow from the inlet to the outlet can be expressed as follows:

$$\Delta t = \frac{V_{\text{chip}}}{Q}$$

where V_{chip} is the internal volume of the chip model and Q is the volumetric flow rate of the fluid. And the improvement rate of mass transfer was obtained by comparing with the simulated reaction volume in the absence of the V-structure under the same conditions.

2.6. Study of steady-state kinetics in the microfluidic chip

To investigate the feasibility of the V-shaped structure in enhancing the catalytic efficiency of nanozymes, the chromogenic reaction catalyzed by the $\text{Fe}_3\text{O}_4/\text{Au}$ nanozyme was built in the chip with or without the optimized corresponding V-structure to obtain the steady-state kinetics parameters. Under the attraction of the gradient magnetic field between the nickel lattices which was induced by a pair of permanent magnets, a magnetic nanozyme array consisting of $\text{Fe}_3\text{O}_4/\text{Au}$ NPs (about 30 μg) was formed at the bottom of the microchannel to react with 120 μL of chromogenic substrates which flowed at $18 \mu\text{L min}^{-1}$ (0.2 M pH = 4 HAc–NaAc buffer containing 4.2 mM TMB and different concentrations of H_2O_2). Then, 30 μL of the chromogenic products flowing out of the channel was collected and the remaining solution was used for the next injection for the catalytic reaction. The process was repeated for 4 cycles to collect chromogenic products which were catalyzed for different times. With an equal

volume of stop solution (2 M H_2SO_4) added, the chromogenic products turned yellow and were tested on a UV-vis spectrophotometer to determine the absorbance at 450 nm. The initial reaction rate ($\mu\text{M s}^{-1}$) of the catalytic reaction at different concentrations of H_2O_2 inside the chip was obtained by fitting the A_{450} and the time for the substrate to flow through the chip and converted by Lambert Beer's law: $A = \varepsilon bc$, where $\varepsilon = 59\,000 \text{ (L mol}^{-1} \text{ cm}^{-1})$ for yellow oxTMB (two electron oxidation).⁴⁰ The kinetic parameters of $\text{Fe}_3\text{O}_4/\text{Au}$ NPs in the microfluidic chip with or without the optimized corresponding V-structure were calculated according to the Michaelis–Menten equation:

$$\nu = V_{\text{max}}[S]/(K_M + [S])$$

where ν is the initial reaction rate, V_{max} is the maximum reaction rate, $[S]$ is the substrate concentration, and K_M is the Michaelis constant. For comparison, the kinetic experiments were conducted under the same conditions using the microplate reader, with the only difference being that the concentration of H_2O_2 was changed to 150–800 mM.

2.7. Computational simulations of the V-corresponding array

A surface binding reaction model was built to illustrate the impact of the V-structure on the binding process between the substrates and the active sites on the surface of the nanozymes inside the corresponding array. The substrate solution set at 100 μM flowed into the microchannel at $2 \mu\text{L min}^{-1}$. The diffusion coefficient was set to $10^{-10} \text{ m}^2 \text{ s}^{-1}$. The concentration of binding sites on the surface of the stacked microsphere models was set to $10^{-7} \text{ mol m}^{-2}$. The k_{ads} was set to $4.0 \times 10^4 \text{ m}^3 \text{ (mol s)}^{-1}$ and the k_{des} was set to $3.0 \times 10^{-4} \text{ s}^{-1}$. By solving the Navier–Stokes equations, the diffusion–convection equations and the general-form boundary partial differential equations, the substrate concentration distribution, the reaction rate and the concentration of the binding products on the surface of the stacked microspheres inside the array at different time points as well as when the reaction reached a steady state were obtained, respectively.

2.8. Synthesis of the $\text{Fe}_3\text{O}_4/\text{Au}$ -aptamer probe

In order to introduce a molecular recognition element for biosensing, the thiol-functionalized specific aptamer of *S. typhimurium* was covalently conjugated onto the $\text{Fe}_3\text{O}_4/\text{Au}$ NPs by Au–S bond. To reduce the modified thiol group on the aptamer, 1 μL of 0.5 M freshly prepared TCEP solution was added into 20 μL of 10 μM aptamer and left at room temperature for 30 min. The aptamer solution was further heated at 95°C , cooled to 0°C for 5 min and incubated at room temperature for another 5 min to fold into a specific spatial structure for later use. 2 mg of $\text{Fe}_3\text{O}_4/\text{Au}$ NPs was mixed with 20 μL of 10 μM 5'-thiol-modified aptamer at 250 rpm overnight. The obtained $\text{Fe}_3\text{O}_4/\text{Au}$ -aptamer probe was dispersed in sterile ultrapure water at 4°C .

2.9. Steady-state kinetic study of $\text{Fe}_3\text{O}_4/\text{Au}$ -aptamer NPs and $\text{Fe}_3\text{O}_4/\text{Au}$ -aptamer@*S. typhimurium* complexes

To verify the inhibition of the peroxidase-like activity of the $\text{Fe}_3\text{O}_4/\text{Au}$ -aptamer NPs with the addition of the target bacteria,



the 0.2 mg mL^{-1} $\text{Fe}_3\text{O}_4/\text{Au}$ -aptamer NPs were incubated with *S. typhimurium* (10^6 CFU mL^{-1}) for 10 min at room temperature. The obtained $\text{Fe}_3\text{O}_4/\text{Au}$ -aptamer@*S. typhimurium* complexes were magnetically washed three times with ultrapure water and resuspended to 0.5 mg mL^{-1} . Subsequently, the steady-state kinetics of the $\text{Fe}_3\text{O}_4/\text{Au}$ -aptamer NPs and the $\text{Fe}_3\text{O}_4/\text{Au}$ -aptamer@*S. typhimurium* complexes were measured with $50 \mu\text{g mL}^{-1}$ of nanoparticles in 0.2 M HAc–NaAc buffer ($\text{pH} = 4$). The concentration of H_2O_2 was fixed at 200 mM when the TMB concentration was varied and the TMB concentration was fixed at $525 \mu\text{M}$ when the H_2O_2 concentration was varied, conversely. The absorbance of oxTMB at 652 nm was recorded every 30 s for 3 min at 37°C using a microplate reader to obtain the initial reaction rate (nM s^{-1}), which was converted by Lambert Beer's law: $A = \varepsilon bc$, where $\varepsilon = 39\,000 \text{ (L mol}^{-1} \text{ cm}^{-1})$ for blue oxTMB (one electron oxidation). The kinetic parameters of the $\text{Fe}_3\text{O}_4/\text{Au}$ -aptamer NPs and the $\text{Fe}_3\text{O}_4/\text{Au}$ -aptamer@*S. typhimurium* complexes were calculated according to the Michaelis–Menten equation.

2.10. Analytical performance of the microfluidic biosensor

The microfluidic chip and the $\text{Fe}_3\text{O}_4/\text{Au}$ -aptamer probe were blocked with 1% BSA for 30 min to minimize nonspecific adsorption before use. The 0.2 mg mL^{-1} $\text{Fe}_3\text{O}_4/\text{Au}$ -aptamer

NPs and *S. typhimurium* with different concentrations from 10^2 to 10^7 CFU mL^{-1} were simultaneously injected into the serpentine mixing channel at a flow rate of $5 \mu\text{L min}^{-1}$ by a precise syringe pump. After they were fully incubated in the mixing zone, the formed $\text{Fe}_3\text{O}_4/\text{Au}$ -aptamer@*S. typhimurium* complexes were captured by the gradient magnetic field between the nickel lattices for 10 min . After washing with PBST solution (containing 0.05% Tween-20) at $2 \mu\text{L min}^{-1}$ for 5 min , $35 \mu\text{L}$ of chromogenic substrates (0.2 M $\text{pH} = 4$ HAc–NaAc buffer containing 3.5 mM TMB and 817 mM H_2O_2) was loaded into the detection chamber for later use. After 2 cycles for back-and-forth movement controlled by the precise syringe pump, the chip was inserted into a dark box containing batteries ($1.5 \text{ V} \times 2$) and a white-light LED (1 W) to eliminate imaging interference. The color change of the chromogenic substrates was recorded by a smartphone and the gray value in the R channel of the images was further analyzed by ImageJ software.

3. Results and discussion

3.1. Characterization of the synthesized nanomaterials

As shown in the TEM image of the synthesized $\text{Fe}_3\text{O}_4/\text{Au}$ NPs, Au NPs were successfully coated on the surface of Fe_3O_4 clusters by an *in situ* reduction method (Fig. 1A). The average

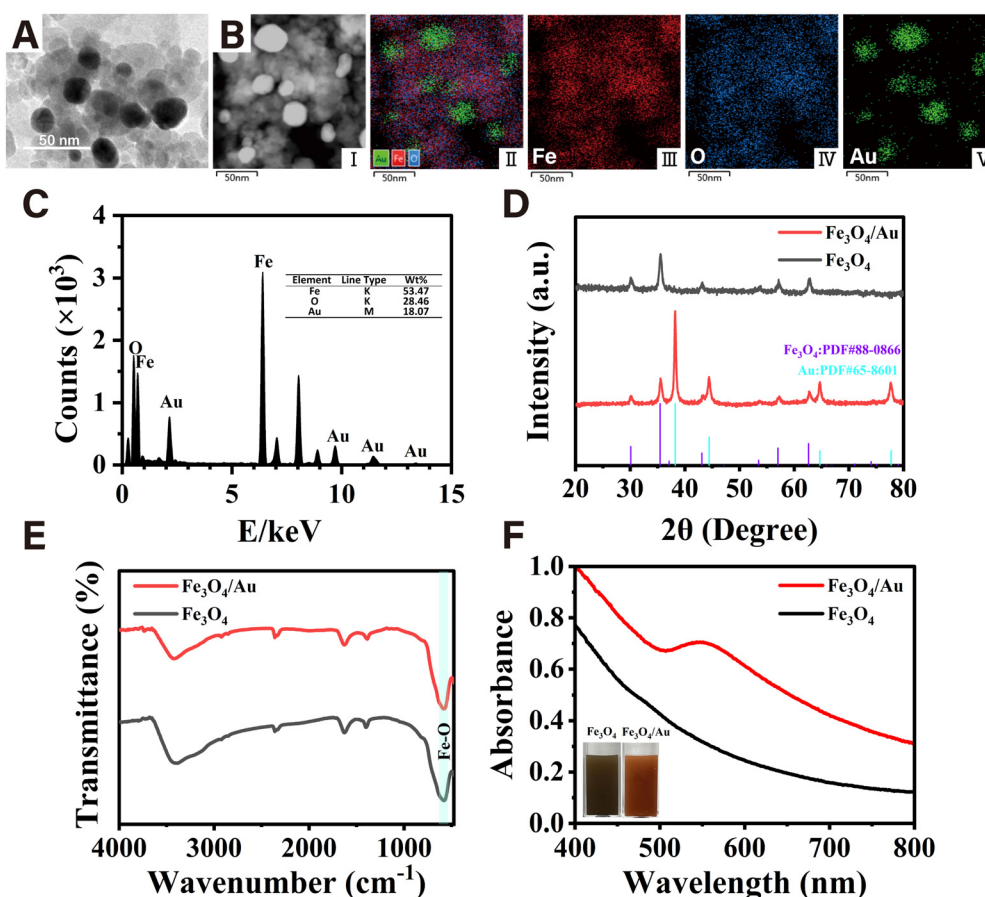


Fig. 1 (A) TEM image of $\text{Fe}_3\text{O}_4/\text{Au}$ NPs. (B) HAADF-STEM image and corresponding TEM elemental mappings of $\text{Fe}_3\text{O}_4/\text{Au}$ NPs. (C) EDS spectrum of $\text{Fe}_3\text{O}_4/\text{Au}$ NPs. (D) XRD patterns of Fe_3O_4 NPs and $\text{Fe}_3\text{O}_4/\text{Au}$ NPs. (E) FT-IR spectra of Fe_3O_4 NPs and $\text{Fe}_3\text{O}_4/\text{Au}$ NPs. (F) UV-vis absorption spectra of Fe_3O_4 NPs and $\text{Fe}_3\text{O}_4/\text{Au}$ NPs. Insert: the photos of water dispersion of Fe_3O_4 NPs and $\text{Fe}_3\text{O}_4/\text{Au}$ NPs.



hydrated particle size of the synthesized nanomaterials increased from 152.8 nm (Fe_3O_4 NPs) to 190.0 nm ($\text{Fe}_3\text{O}_4/\text{Au}$ NPs) (Fig. S1, ESI†). In addition, the high-angle annular dark field scanning transmission electron microscopy (HAADF-STEM) and the corresponding EDS mapping showed that the Fe, O, and Au elements uniformly distributed on the surface of $\text{Fe}_3\text{O}_4/\text{Au}$ NPs, with a weight fraction determined to be 53.47%, 28.46%, and 18.07% respectively (Fig. 1B and C). As shown in Fig. 1D, typical XRD diffraction peaks of Fe_3O_4 NPs and $\text{Fe}_3\text{O}_4/\text{Au}$ NPs at 30.1° , 35.4° , 43.1° , 57.0° and 62.6° can be indexed to the (220), (311), (400), (511) and (440) crystal planes of Fe_3O_4 (PDF#88-0866). The successful immobilization of Au on the Fe_3O_4 NPs was further confirmed by the additional diffraction peaks at 38.2° , 44.4° , 64.7° and 77.6° , which were indexed to the (111), (200), (220), and (311) crystal planes of Au (PDF#65-8601). According to the FT-IR spectra of Fe_3O_4 NPs and $\text{Fe}_3\text{O}_4/\text{Au}$ NPs (Fig. 1E), they both showed a significant absorption peak at 586 cm^{-1} which was ascribed to the Fe–O stretching vibrations. As shown in Fig. 1F, the $\text{Fe}_3\text{O}_4/\text{Au}$ NPs exhibited an UV-visible absorption peak at 550 nm after the *in situ* growth of Au NPs on the surface of Fe_3O_4 NPs, presenting a deep red color.

3.2. POD-like catalytic activity of $\text{Fe}_3\text{O}_4/\text{Au}$ NPs

The peroxidase-like activity of the $\text{Fe}_3\text{O}_4/\text{Au}$ NPs was tested by measuring the UV-vis absorption spectra in the different reaction systems. As shown in Fig. S2 (ESI†), when the $\text{Fe}_3\text{O}_4/\text{Au}$ NPs, H_2O_2 , and TMB were present in the reaction system simultaneously, an obvious absorption peak of oxTMB appeared at

652 nm. The prepared $\text{Fe}_3\text{O}_4/\text{Au}$ NPs can catalytically oxidize TMB in the presence of H_2O_2 , suggesting their peroxidase-like activity. The catalytic activity of the $\text{Fe}_3\text{O}_4/\text{Au}$ NPs was significantly influenced by the pH in the catalytic system. As shown in Fig. S3 (ESI†), when the pH value was 4, the absorbance of oxTMB at 652 nm reached the maximum. Thus, the HAc–NaAc buffer (pH = 4) was used in all experiments. In addition, the storage stability of the $\text{Fe}_3\text{O}_4/\text{Au}$ NPs at room temperature and 4°C was investigated. After 5 weeks of storage, the relative activity of the $\text{Fe}_3\text{O}_4/\text{Au}$ NPs remained 96% at 4°C and 94% at room temperature, respectively, which indicated the good storage stability of the synthesized $\text{Fe}_3\text{O}_4/\text{Au}$ NPs (Fig. S4, ESI†).

3.3. Optimization of the V-shaped superstructure

The staggered array structure at the bottom could realize lateral mass transfer, while the additional existence of the V-superstructure played a role of transferring the solution from the top of the channel to the corresponding array in the vertical direction. The influence of the detailed parameters of the V-structure including the arrangement pattern, the angle, the arm width, and the height as well as the total height of the channel on the mass transfer efficiency were optimized by simulating the upper surface pressure of the array and the volume of fluid entering a lattice unit. As shown in Fig. 2A, when the upper structures were arranged in a completely staggered pattern, with no adjacent structures being parallel, the fluid could generate the maximum average pressure on the array surface, increasing by 109% compared to the chip without the V-structure. As shown in Fig. 2B, the simulation results of average pressure on

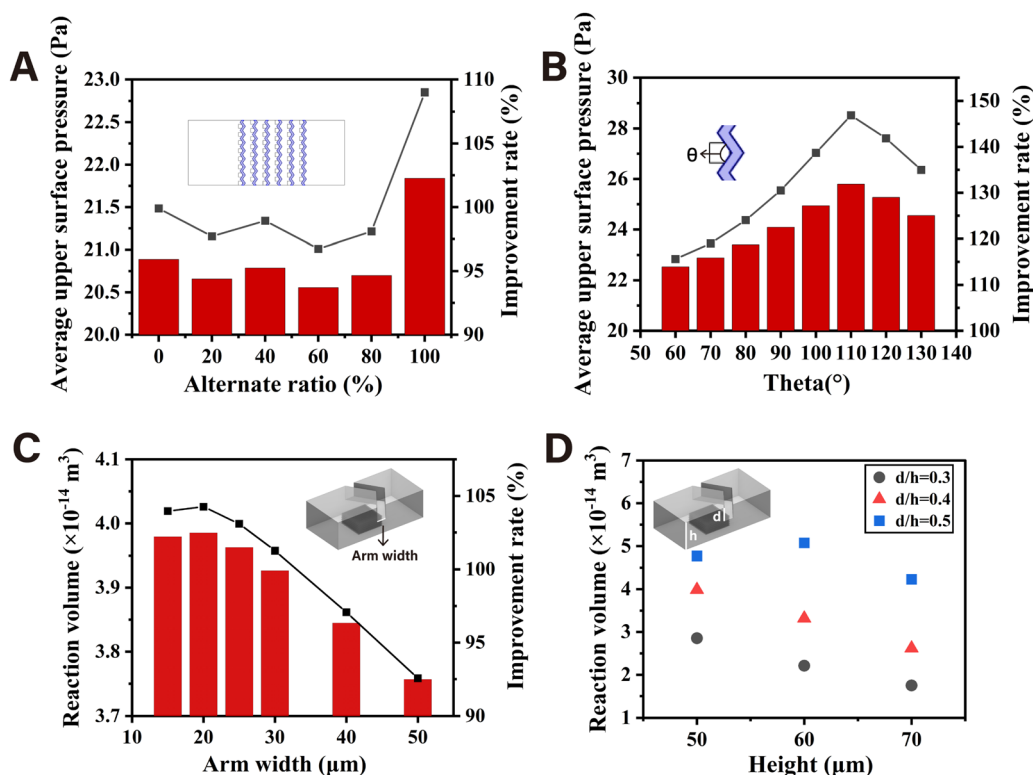


Fig. 2 Simulation of the effects of alternative ratio (A), angle (B), arm width (C), and height (D) of the V-structure.



the upper surface of the array increased consecutively when the angle of the upper V-shaped structure increased from 50 to 110°. When the angle increased further beyond 110°, the average upper surface pressure began to decrease. Thus, the optimal angle of the V-structure was 110°, generating upper surface pressure almost 2.5 times higher than that without the corresponding V-structure. Based on the above conditions, the arm width and height of the V-structure, as well as the total height of the channel were optimized based on the volume of fluid entering a single lattice unit consisting of stacking microspheres during the time from the inlet to the outlet. Fig. 2C shows that when the width was 20 μm , the volume of fluid entering the lattice unit to react with microspheres (V_{total}) reached its maximum. Thus, 20 μm was selected as the optimal arm width of the V-structure. Finally, the total height of the channel and the proportion of the V-structure to it (d/h) were optimized in the same way. As shown in Fig. 2D, when the channel height is 60 μm and the proportion of the V-structure is 0.5, the reaction volume of fluid entering the lattice unit (V_{total}) was highest, demonstrating a 214.5% improvement rate to the 60- μm -high chip without the V-structure. The optimized parameters and microscopic image of the V-structure are shown in Fig. S5 (ESI†).

3.4. Catalytic efficiency enhancement of nanozymes mediated by the V-structured chip

The chromogenic reaction catalyzed by $\text{Fe}_3\text{O}_4/\text{Au}$ NPs in the presence of TMB and different concentrations of H_2O_2 was carried out in the microfluidic chips with different structures and open reactor to compare the peroxidase-like kinetic performance. The magnetic nanozyme array consisting of $\text{Fe}_3\text{O}_4/\text{Au}$ NPs formed under the attraction of the gradient magnetic field between the nickel lattices is shown in Fig. S6 (ESI†). As shown in Fig. 3A, whether the microfluidic chip was structured or unstructured, the absorbance increased continuously with the increasing H_2O_2 concentration from 2 mM to 20 mM in the same reaction cycle. Likewise, at the same concentration of H_2O_2 , the absorbance increased with the increase of the number of reaction cycles. As expected, the absorbance values of the V-structured group were obviously higher than those of the unstructured group under the

same H_2O_2 concentration and reaction cycle due to the greatly improved mass transfer of the substrate solution which was mediated by the corresponding V-structure. The steady-state kinetic parameters were studied in chips and open reactor with H_2O_2 as the substrate by fitting the Michaelis-Menten curve. As shown in Fig. 3B, the apparent Michaelis constant ($K_{\text{M,app}}$) of the $\text{Fe}_3\text{O}_4/\text{Au}$ nanozyme with H_2O_2 as the substrate decreased from 284.89 mM in the open system to 3.44 mM and 3.47 mM in the microfluidic chips. In addition, the microfluidic chip with or without the V-structure exhibited an apparent maximum reaction rate ($V_{\text{max,app}}$) of the $\text{Fe}_3\text{O}_4/\text{Au}$ nanozyme which was more than 4 times or 2 times higher than that of 0.53 $\mu\text{M s}^{-1}$ in the open reactor. Thus, according to $k_{\text{cat}} = V_{\text{max}}/[E]$, where $[E]$ is the same concentration of nanozyme, an improvement in catalytic efficiency ($k_{\text{cat}}/K_{\text{M}}$) of two orders of magnitude was obtained in the microfluidic chip compared with that of the open reactor. This can be explained as that every single lattice consisting of $\text{Fe}_3\text{O}_4/\text{Au}$ nanozyme could act as a spatially confined microreactor. The limited diffusion distance made it easier for the substrate to diffuse and adsorb to the surface of the active sites of the nanozyme, enhancing the apparent affinity between them. Furthermore, the continuous flowing of the substrate not only maintained a high concentration gradient but also ensured the timely release of the products, thus exhibiting a faster reaction rate and a significant increase in catalytic efficiency. Moreover, the Michaelis-Menten steady-state kinetics results demonstrated that the $\text{Fe}_3\text{O}_4/\text{Au}$ NPs arrayed under the corresponding V-structure exhibited a superior catalytic performance to that without the V-structure, as evidenced by the increase in the apparent maximum reaction rate ($V_{\text{max,app}}$) from 1.23 $\mu\text{M s}^{-1}$ to 2.38 $\mu\text{M s}^{-1}$. Thus, a 1.95 times higher catalytic efficiency ($k_{\text{cat}}/K_{\text{M}}$) of $\text{Fe}_3\text{O}_4/\text{Au}$ nanozyme was obtained in the presence of the optimal V-structure, which was mainly attributed to the acceleration of the catalytic reaction.

The simulation of the binding process between the substrate and the active sites on the surface of the stacking nanozyme particles provided a more intuitive confirmation of the enhancement of reaction efficiency inside the array due to the existence of the corresponding upper V-structure. As can be

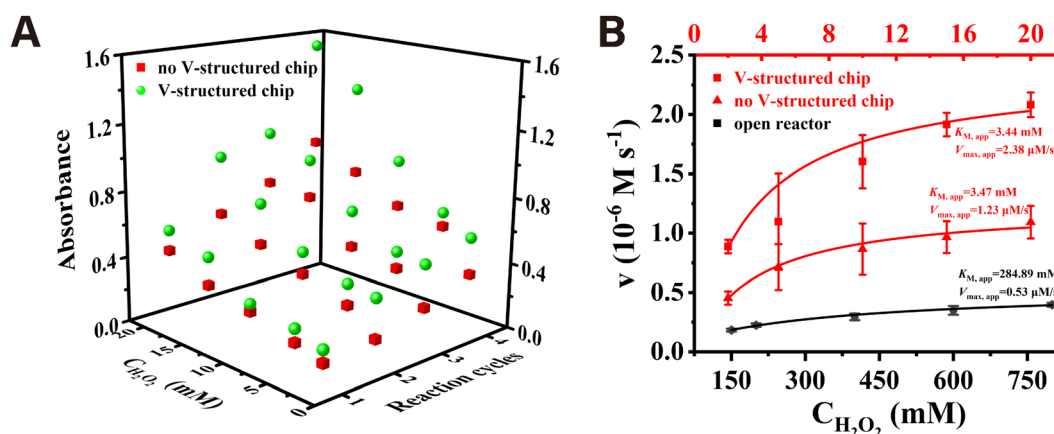


Fig. 3 (A) Absorbance of chromogenic products at 450 nm in the chip with or without the V-structure at different H_2O_2 concentrations and reaction cycles. (B) Steady-state kinetic assay in chips and open reactor with H_2O_2 as the substrate.

seen from Fig. S7A (ESI[†]), there was a higher substrate concentration evidently inside the lattice unit consisting of microsphere models corresponding to the V-shaped structure under the same reaction condition settings. In the initial stage of the reaction, the lattice unit corresponding to the V-shaped structure generated a relatively higher binding rate on the external surfaces. As the binding sites on the external surface gradually became saturated, the maximum reaction rate surfaces moved from the outside to the inside. However, the lattice unit without the corresponding V-shaped structure maintained a relatively lower reaction rate throughout the reaction process (Fig. S7B, ESI[†]).

The concentration distribution of the reaction products on the surface of the stacked microsphere models could indicate the utilization rate of the active sites on the surface of nanozyme particles. As shown in Fig. 4A and B, the concentration of the products on the external surfaces of the lattice unit corresponding to the V-structure was significantly higher at any time points as the reaction progressed, which was ascribed to the increased local concentration of substrate inside the array. Moreover, the reaction proceeded more evenly on the surface of each microsphere model due to the uniform distribution of the fluid on each direction promoted by the V-structure. When the two reaction models reached a steady state respectively, the lattice unit corresponding to the V-structure demonstrated a higher reaction efficiency (Fig. 4C and D).

On the one hand, the efficient mass transfer of the substrate under the corresponding V-structure in the microchannel could increase the local substrate concentration among the stacked

$\text{Fe}_3\text{O}_4/\text{Au}$ nanozyme particles, thereby accelerating the catalytic reaction. On the other hand, the more uniform distribution of the substrate molecules at each direction of the array allowed for more efficient utilization of the active sites of the nanozyme in the catalysis of substrates.

Therefore, the efficient catalytic model of the V-nanozyme array consisting of the $\text{Fe}_3\text{O}_4/\text{Au}$ NPs was used as a signal amplification strategy for sensitive biosensing.

3.5. Characterization of $\text{Fe}_3\text{O}_4/\text{Au}$ -aptamer probes

For the specific identification and capture of *S. typhimurium*, the thiol-functionalized specific aptamer of *S. typhimurium* was covalently conjugated to the $\text{Fe}_3\text{O}_4/\text{Au}$ NPs *via* Au-S bonds. The hydrated particle size and the zeta potential were measured by DLS to verify conjugation of the aptamer. As shown in Fig. S8 (ESI[†]), the zeta potential of the $\text{Fe}_3\text{O}_4/\text{Au}$ NPs was 16.9 mV while the $\text{Fe}_3\text{O}_4/\text{Au}$ -aptamer NPs were negatively charged with a zeta potential of -32.5 mV due to negative charges carried by DNA oligonucleotides. The average particle size of $\text{Fe}_3\text{O}_4/\text{Au}$ NPs increased from 190.0 nm to 420.0 nm after conjugation of the aptamer. The results above evidenced the successful conjugation of the aptamer and the amount of DNA oligonucleotides per milligram $\text{Fe}_3\text{O}_4/\text{Au}$ NPs were further estimated as $(5.32 \pm 0.36) \times 10^{13}$ ($N = 3$) using a UV-visible spectrophotometer (Fig. S9, ESI[†]).

3.6. Feasibility study of this colorimetric method

To demonstrate that the peroxidase-like activity of the $\text{Fe}_3\text{O}_4/\text{Au}$ -aptamer NPs was able to be inhibited *via* the formation of

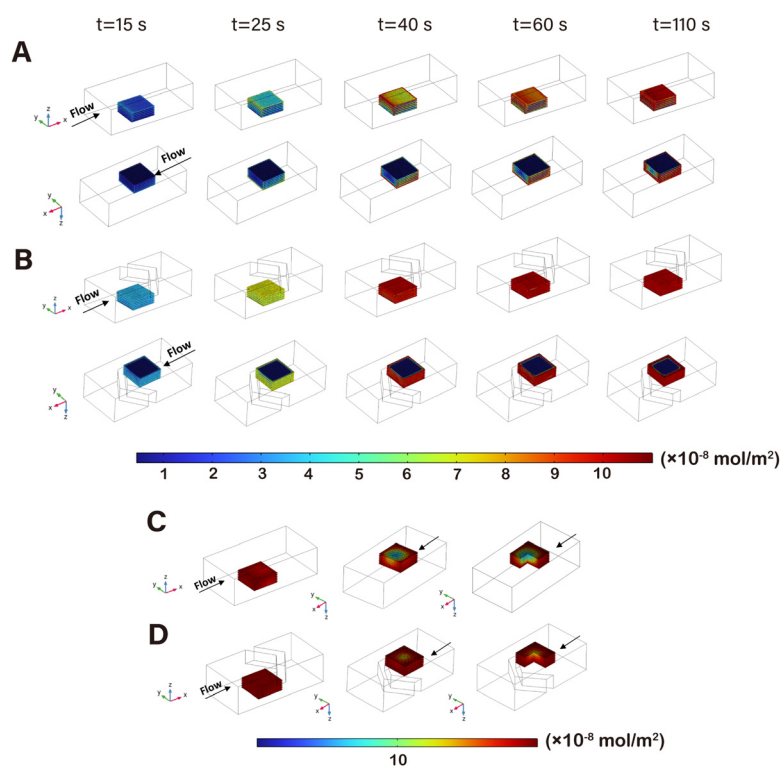


Fig. 4 Simulation of surface concentration of products in chip models without (A) or with (B) V-superstructure at different time points. Simulation of surface concentration of products in chip models without (C) or with (D) V-superstructure at a steady state.



aptamer-*S. typhimurium* complexes on the surface, *S. typhimurium* was incubated with the $\text{Fe}_3\text{O}_4/\text{Au}$ NPs and the $\text{Fe}_3\text{O}_4/\text{Au}$ -aptamer NPs respectively under the same conditions. As shown in Fig. 5A, the absorption peak of oxTMB at 652 nm decreased obviously with the addition of *S. typhimurium* for $\text{Fe}_3\text{O}_4/\text{Au}$ -aptamer NPs, which only decreased slightly as for the $\text{Fe}_3\text{O}_4/\text{Au}$ NPs due to the nonspecific adsorption.

Different concentrations of *S. typhimurium* (50 μL , ranging from 10^3 to 10^7 CFU mL^{-1}) were mixed with 100 μL of 0.5 mg mL^{-1} $\text{Fe}_3\text{O}_4/\text{Au}$ -aptamer NPs respectively on a vortex mixer for 10 min. The $\text{Fe}_3\text{O}_4/\text{Au}$ -aptamer@*S. typhimurium* complexes were collected magnetically, followed by the addition of 210 μL of chromogenic solution (HAc–NaAc buffer containing 1 mM TMB and 233 mM H_2O_2). After reaction at room temperature for 2 min, the UV-vis spectra in the range of 550–750 nm were measured individually. As shown in Fig. 5B, the absorption peak at 652 nm declined gradually with the increase of *S. typhimurium* concentration. These results verified the feasibility of the proposed method.

Furthermore, the typical Michaelis–Menten curves and Lineweaver–Burk plots of the $\text{Fe}_3\text{O}_4/\text{Au}$ -aptamer NPs in the presence and absence of *S. typhimurium* were drawn to obtain the K_M and V_{max} . As shown in Fig. S10 (ESI[†]), the K_M with TMB as the substrate was 0.776 mM for the $\text{Fe}_3\text{O}_4/\text{Au}$ -aptamer NPs and 0.918 mM for the $\text{Fe}_3\text{O}_4/\text{Au}$ -aptamer@*S. typhimurium* complexes. When the substrate was H_2O_2 , the K_M was 479.8 mM for the $\text{Fe}_3\text{O}_4/\text{Au}$ -aptamer NPs and 509.2 mM for the $\text{Fe}_3\text{O}_4/\text{Au}$ -aptamer@*S. typhimurium* complexes.

The increased K_M value indicated the decrease of affinity, which could be attributed to the inaccessibility of substrates to catalytic active sites under the formation of an aptamer-*S. typhimurium* blocking layer on the surface.

3.7. Condition screening for the microfluidic biosensing

The $\text{Fe}_3\text{O}_4/\text{Au}$ -aptamer NPs and *S. typhimurium* were firstly injected into the serpentine mixing zone simultaneously to

form the $\text{Fe}_3\text{O}_4/\text{Au}$ -aptamer@*S. typhimurium* complexes. After the mixing zone, the magnetic complexes were staggered in the enrichment and catalyzing zone, followed by the catalytic reaction with the flowing chromogenic substrate. A photo of the integrated microfluidic chip is shown in Fig. S11 (ESI[†]). In order to obtain the maximum change in colorimetric signal after the addition of *S. typhimurium*, the concentration of $\text{Fe}_3\text{O}_4/\text{Au}$ -aptamer NPs was optimized. 100 μL of $\text{Fe}_3\text{O}_4/\text{Au}$ -aptamer NPs at different concentrations were mixed with 100 μL of *S. typhimurium* (10^6 CFU mL^{-1}) using a vortex mixer for 10 minutes. After the complexes were collected magnetically, 210 μL of HAc–NaAc buffer containing 1 mM TMB and 233 mM H_2O_2 was added for chromogenic reaction for 2 min. As shown in Fig. 6A, the normalized ΔAbs intensity ($\Delta\text{Abs} = A_0 - A$, where A_0 and A represent the absorbance at 652 nm in the absence and presence of *S. typhimurium*, respectively) first increased and then decreased within the range of 0.05–0.4 mg mL^{-1} for the $\text{Fe}_3\text{O}_4/\text{Au}$ -aptamer NP concentration. As a result, 0.2 mg mL^{-1} of $\text{Fe}_3\text{O}_4/\text{Au}$ -aptamer NPs was adopted as the optimal concentration.

In addition, the enrichment efficiency of the magnetic complexes in the staggered nickel patterns was evaluated. The characteristic absorption of $\text{Fe}_3\text{O}_4/\text{Au}$ NPs at 550 nm was positively correlated with the concentration (Fig. S12, ESI[†]). 0.1 mg mL^{-1} of $\text{Fe}_3\text{O}_4/\text{Au}$ NPs was injected into the enrichment zone under different flow rates, and the enrichment efficiency was calculated by $(A_{\text{inlet}} - A_{\text{outlet}})/A_{\text{inlet}} \times 100\%$, where A is the absorbance measured at 550 nm. A lower flow rate made it easier to be captured in the magnetic field. As shown in Fig. 6B, with the increasing flow rate from 6–20 $\mu\text{L min}^{-1}$, the enrichment efficiency decreased gradually, remaining in the range of 86–96%.

Furthermore, the flow rate for the injection of each single inlet in the mixing zone was investigated. On the basis of the optimization mentioned above, 0.2 mg mL^{-1} $\text{Fe}_3\text{O}_4/\text{Au}$ -aptamer NPs and *S. typhimurium* (10^6 CFU mL^{-1}) were injected into the serpentine chip simultaneously at different flow rates. The magnetic

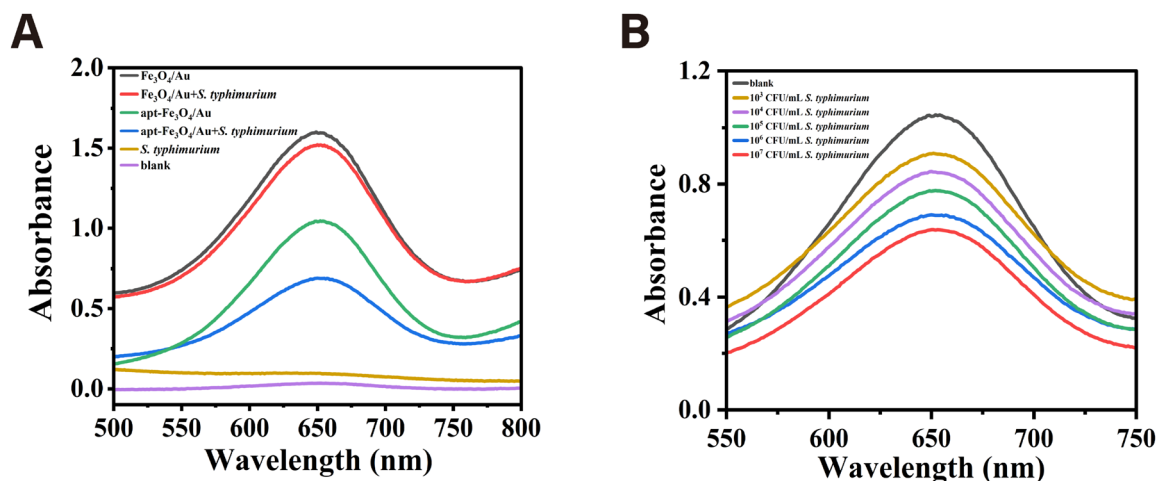


Fig. 5 (A) UV-vis absorption spectra of the reaction solutions with different materials (50 μg $\text{Fe}_3\text{O}_4/\text{Au}$ NPs or $\text{Fe}_3\text{O}_4/\text{Au}$ -aptamer NPs, 50 μL of 10^6 CFU mL^{-1} *S. typhimurium*) added in 210 μL HAc–NaAc buffer (pH = 4, containing 1 mM TMB and 233 mM H_2O_2). (B) UV-vis absorption spectra of the reaction solutions with 50 μg $\text{Fe}_3\text{O}_4/\text{Au}$ -aptamer NPs and 50 μL of different concentrations of *S. typhimurium* added in 210 μL HAc–NaAc buffer (pH = 4, containing 1 mM TMB and 233 mM H_2O_2).



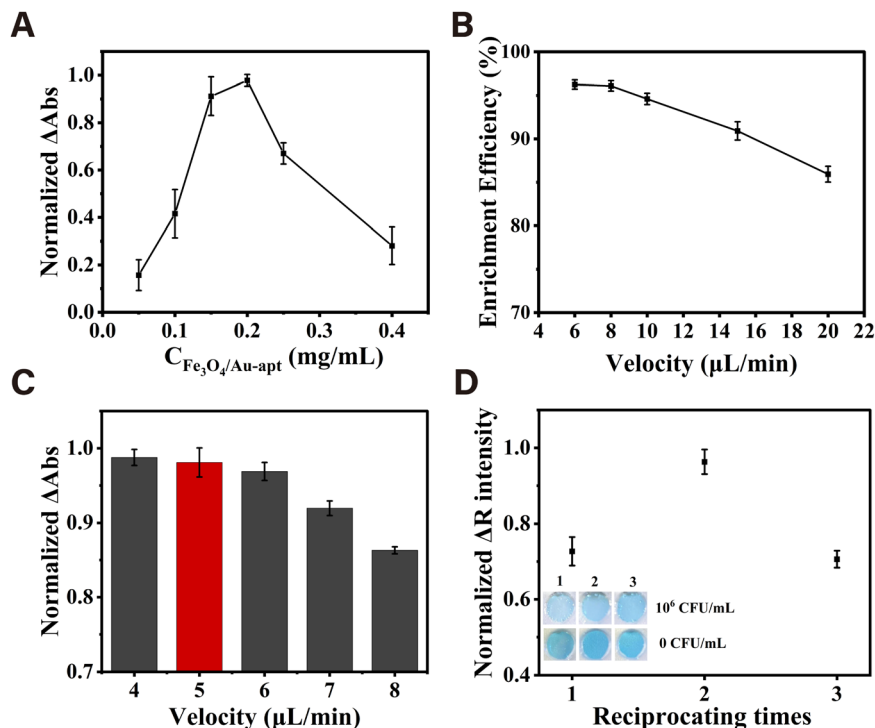


Fig. 6 Optimization of biosensing conditions in the microfluidic platform. (A) Concentration of the $\text{Fe}_3\text{O}_4/\text{Au}$ -aptamer NPs. (B) Flow rate for the enrichment of the $\text{Fe}_3\text{O}_4/\text{Au}$ NPs. (C) Flow rate for the mixing of the $\text{Fe}_3\text{O}_4/\text{Au}$ -aptamer NPs and *S. typhimurium*. (D) Reciprocating times of the chromogenic substrates (35 μL of HAC–NaAc buffer containing 3.5 mM TMB and 817 mM H_2O_2).

complexes were collected at the outlet and further washed with ultrapure water magnetically. The ΔAbs intensity at 652 nm was measured by an UV-vis spectrophotometer. As shown in Fig. 6C, the normalized ΔAbs intensity increased gradually and tended to be stable with the decrease of the flow rate. Considering the detection time, 5 $\mu\text{L}/\text{min}$ was selected as the flow rate for the injection of each single inlet in the mixing zone. To produce sensitive color signals, the reciprocating (back-and-forth movement) times of chromogenic substrates in the detection chamber were optimized according to ΔR value ($\Delta R = R - R_0$), where R and R_0 are obtained in the presence and absence of *S. typhimurium* (10^6 CFU mL^{-1}). After 3 cycles of reciprocation of the chromogenic substrates (HAC–NaAc buffer containing 3.5 mM TMB and 817 mM H_2O_2 , 35 μL) at 15 $\mu\text{L}/\text{min}$ with the assistance of a precise syringe pump, the color change at the end of each cycle of reciprocation was recorded by a smartphone and quantified by ImageJ software. As shown in Fig. 6D, the ΔR value reached the highest through 2 cycles of reciprocation for the certain concentration of chromogenic substrates. Therefore, 2 cycles of reciprocation were chosen in this work to ensure appropriate chromogenic time.

3.8. Analytical performance of this colorimetric method on the microfluidic platform

Under optimal conditions, 10-fold serial dilutions of *S. typhimurium* ranging from 10^2 to 10^7 CFU mL^{-1} were tested to establish the calibration curve between the ΔR value and the concentration of *S. typhimurium*. As can be seen in Fig. 7A, the ΔR value increased linearly with the logarithmic concentration of *S. typhimurium* ($\log C$, CFU mL^{-1}) in the range of 10^2 – 10^7 CFU mL^{-1} , which could be

described as the following regression equation: $\Delta R = 17.16 \log C - 21.17$ ($R^2 = 0.982$). Based on 3 times the signal-to-noise ratio, the limit of detection (LOD) was calculated to be 5.6 CFU mL^{-1} . To evaluate the specificity of this proposed method, the target bacteria (*S. typhimurium*) at 10^6 CFU mL^{-1} , non-target bacteria (*P. aeruginosa*, *L. monocytogenes*, *E. coli* O157:H7 and *S. aureus*) at a concentration of 10^8 CFU mL^{-1} and their mixture at 10^6 CFU mL^{-1} were detected using this proposed method on the microfluidic platform. As shown in Fig. 7B, only the target bacteria and the mixture showed obvious decrease in the R value, indicating the desirable specificity of this method. Compared with other reported methods, this proposed colorimetric method for *S. typhimurium* detection on the integrated microfluidic platform showed a comparable detection limit and shorter detection time (Table S1, ESI†).

The practical applicability of the integrated microfluidic platform was evaluated by detecting the target bacteria spiked in water, milk, and chicken meat samples. Table 1 showed that the recoveries for the spiked samples were in the range of 95.5–114.7% and the relative standard deviations (RSDs) were less than 12.5%, indicating good applicability of this proposed colorimetric method on the microfluidic platform for *S. typhimurium* detection in real samples.

On this integrated microfluidic platform for biosensing of *S. typhimurium*, the magnetism-controlled V-structured chip with enhanced mass transfer characteristics was introduced for signal amplification which also eliminated the need for additional separation steps, achieving sensitive detection of *S. typhimurium* within 30 minutes. Moreover, smartphone-based signal readout further enhanced the portability of this microfluidic platform,



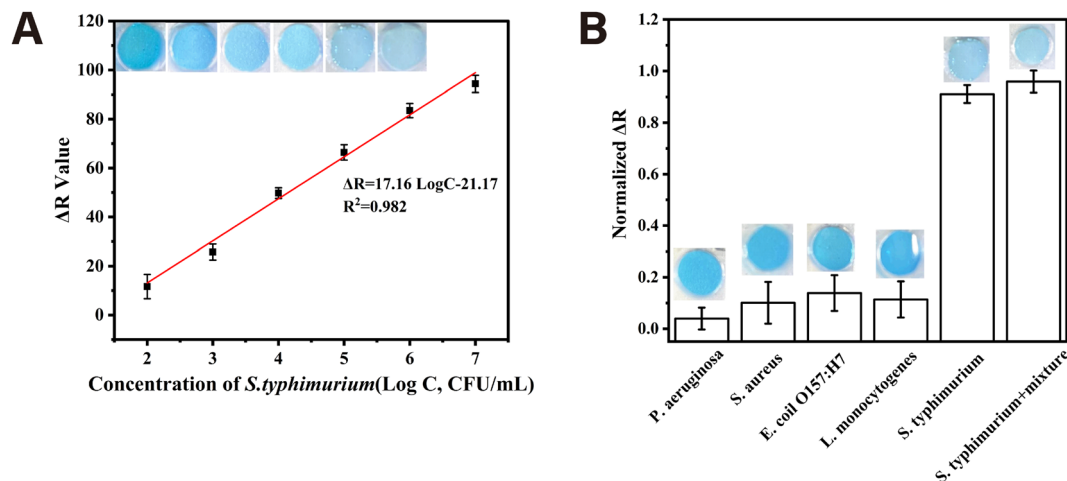


Fig. 7 Analytical performance of the microfluidic platform. (A) Calibration curve of this colorimetric method. (B) Specificity of this colorimetric method.

Table 1 Detection of *S. typhimurium* in spiked samples on the microfluidic platform ($N = 3$)

	Added (CFU mL ⁻¹)	Recovered (CFU mL ⁻¹)	Recovery (%)	RSD (%)
Water1	1.80×10^3	1.72×10^3	95.5	5.5
Water2	1.80×10^4	1.85×10^4	103.0	12.5
Milk1	1.80×10^3	2.07×10^3	114.7	7.0
Milk2	1.80×10^4	1.97×10^4	109.5	9.1
Chicken1	1.80×10^3	1.75×10^3	97.5	11.2
Chicken2	1.80×10^4	1.72×10^4	95.6	7.2

demonstrating practical applicability and promising potential for rapid foodborne pathogen detection.

4. Conclusions

In this work, a kind of V-shaped structure was constructed to enhance the mass transfer of substrate solution towards the corresponding nanozyme array which consisted of stacked Fe₃O₄/Au NPs inside the magnetism-controlled microfluidic chip. A higher local concentration of substrate among the stacked Fe₃O₄/Au nanozyme particles in the array accelerated the catalytic reaction. Moreover, the uniform distribution of the substrate molecules at each direction of the V-corresponding array allowed for more efficient utilization of the active sites of the nanozyme in the catalysis of substrates. Subsequently, the catalytic efficiency (k_{cat}/K_M) of the Fe₃O₄/Au nanozyme arrayed in the microfluidic chip increased by 95.2% in the presence of the optimal V-structure, which was two orders of magnitude higher than that of the open reactor. Furthermore, this strategy was applied as signal amplification for the biosensing of *S. typhimurium* on an integrated microfluidic platform. The entire detection process including incubation, enrichment, catalyzing and signal readout by the smartphone was integrated onto the microfluidic chip, which could be completed in 30 minutes, yielding a detection limit as low as 5.6 CFU mL⁻¹.

Author contributions

Ming-Yue Gao: investigation, validation, methodology, writing – original draft, writing – review & editing. Meng Wang: investigation, writing – review & editing. Yong-Tao Wang: methodology. Zhi-Ling Zhang: methodology, resources, supervision, writing – original draft, writing – review & editing, funding acquisition.

Data availability

The data that support this study have been included as part of the ESI.†

Conflicts of interest

There are no conflicts to declare.

Acknowledgements

This work was supported by the National Natural Science Foundation of China (22274118).

Notes and references

- 1 D. Jiang, D. Ni, Z. T. Rosenkrans, P. Huang, X. Yan and W. Cai, Nanozyme: new horizons for responsive biomedical applications, *Chem. Soc. Rev.*, 2019, **48**, 3683–3704.
- 2 S. Li, L. Shang, B. Xu, S. Wang, K. Gu, Q. Wu, Y. Sun, Q. Zhang, H. Yang, F. Zhang, L. Gu, T. Zhang and H. Liu, A Nanozyme with Photo-Enhanced Dual Enzyme-Like Activities for Deep Pancreatic Cancer Therapy, *Angew. Chem., Int. Ed.*, 2019, **58**, 12624–12631.
- 3 G. Tang, J. He, J. Liu, X. Yan and K. Fan, Nanozyme for tumor therapy: Surface modification matters, *Exploration*, 2021, **1**, 75–89.
- 4 A. F. Baye, H. T. Nguyen and H. Kim, Fe⁰/Fe₃C-assisted Fe₃O₄ redox sites as robust peroxidase mimics for colorimetric detection of H₂O₂, *Sens. Actuator, B*, 2023, **377**, 133097.



- 5 N. Lu, M. Zhang, L. Ding, J. Zheng, C. Zeng, Y. Wen, G. Liu, A. Aldalbahi, J. Shi, S. Song, X. Zuo and L. Wang, Yolk-shell nanostructured $\text{Fe}_3\text{O}_4/\text{C}$ magnetic nanoparticles with enhanced peroxidase-like activity for label-free colorimetric detection of H_2O_2 and glucose, *Nanoscale*, 2017, **9**, 4508–4515.
- 6 R. Zhang, N. Lu, J. Zhang, R. Yan, J. Li, L. Wang, N. Wang, M. Lv and M. Zhang, Ultrasensitive aptamer-based protein assays based on one-dimensional core-shell nanozymes, *Biosens. Bioelectron.*, 2020, **150**, 111881.
- 7 Y. Gao, S. Xu, G. Guo, Y. Li, W. Zhou, H. Li and Z. Yang, $\text{MoO}_3/\text{MIL-125-NH}_2$ with boosted peroxidase-like activity for electrochemical staphylococcus aureus sensing via specific recognition of bacteriophages, *Biosens. Bioelectron.*, 2024, **252**, 116134.
- 8 G. Wu, A. Dilinaer, P. Nie, X. Liu, Z. Zheng, P. Luo, W. Chen, Y. Wu and Y. Shen, Dual-Modal Bimetallic Nanozyme-Based Sensing Platform Combining Colorimetric and Photothermal Signal Cascade Catalytic Enhancement for Detection of Hypoxanthine to Judge Meat Freshness, *J. Agric. Food Chem.*, 2023, **71**, 16381–16390.
- 9 M. Zheng, M. Liu, Z. Song, F. Ma, H. Zhu, H. Guo and H. Sun, High-precision colorimetric-fluorescent dual-mode biosensor for detecting acetylcholinesterase based on a trimetallic nanozyme for efficient peroxidase-mimicking, *J. Mater. Sci. Technol.*, 2024, **191**, 168–180.
- 10 X. Tao, X. Wang, B. Liu and J. Liu, Conjugation of antibodies and aptamers on nanozymes for developing biosensors, *Biosens. Bioelectron.*, 2020, **168**, 112537.
- 11 Y. Gao, Y. Wang, Y. Wang, P. Magaud, Y. Liu, F. Zeng, J. Yang, L. Baldas and Y. Song, Nanocatalysis meets microfluidics: A powerful platform for sensitive bioanalysis, *Trac, Trends Anal. Chem.*, 2023, **158**, 116887.
- 12 J. Wu, X. Wang, Q. Wang, Z. Lou, S. Li, Y. Zhu, L. Qin and H. Wei, Nanomaterials with enzyme-like characteristics (nanozymes): next-generation artificial enzymes (II), *Chem. Soc. Rev.*, 2019, **48**, 1004–1076.
- 13 P. Jin, X. Niu, Z. Gao, X. Xue, F. Zhang, W. Cheng, C. Ren, H. Du, A. Manyande and H. Chen, Ultrafine Platinum Nanoparticles Supported on Covalent Organic Frameworks As Stable and Reusable Oxidase-Like Catalysts for Cellular Glutathione Detection, *ACS Appl. Nano Mater.*, 2021, **4**, 5834–5841.
- 14 M. Wei, J. Lee, F. Xia, P. Lin, X. Hu, F. Li and D. Ling, Chemical design of nanozymes for biomedical applications, *Acta Biomater.*, 2021, **126**, 15–30.
- 15 L. Feng, L. Zhang, S. Zhang, X. Chen, P. Li, Y. Gao, S. Xie, A. Zhang and H. Wang, Plasma-Assisted Controllable Doping of Nitrogen into MoS_2 Nanosheets as Efficient Nanozymes with Enhanced Peroxidase-Like Catalysis Activity, *ACS Appl. Mater. Interfaces*, 2020, **12**, 17547–17556.
- 16 B. Liu and J. Liu, Surface modification of nanozymes, *Nano Res.*, 2017, **10**, 1125–1148.
- 17 Z. Wang, R. Zhang, X. Yan and K. Fan, Structure and activity of nanozymes: Inspirations for de novo design of nanozymes, *Mater. Today*, 2020, **41**, 81–119.
- 18 C. Zeng, N. Lu, Y. Wen, G. Liu, R. Zhang, J. Zhang, F. Wang, X. Liu, Q. Li, Z. Tang and M. Zhang, Engineering Nanozymes Using DNA for Catalytic Regulation, *ACS Appl. Mater. Interfaces*, 2019, **11**, 1790–1799.
- 19 K. Fan, H. Wang, J. Xi, Q. Liu, X. Meng, D. Duan, L. Gao and X. Yan, Optimization of Fe_3O_4 nanozyme activity via single amino acid modification mimicking an enzyme active site, *Chem. Commun.*, 2017, **53**, 424–427.
- 20 M. Li, J. Chen, W. Wu, Y. Fang and S. Dong, Oxidase-like MOF-818 Nanozyme with High Specificity for Catalysis of Catechol Oxidation, *J. Am. Chem. Soc.*, 2020, **142**, 15569–15574.
- 21 N. Zhao, F. E. Yang, C. Y. Zhao, S. W. Lv, J. Wang, J. M. Liu and S. Wang, Construction of pH-Dependent Nanozymes with Oxygen Vacancies as the High-Efficient Reactive Oxygen Species Scavenger for Oral-Administered Anti-Inflammatory Therapy, *Adv. Healthcare Mater.*, 2021, **10**, 2101618.
- 22 Y. Liu, Y. Xiang, Y. Zhen and R. Guo, Halide Ion-Induced Switching of Gold Nanozyme Activity Based on Au–X Interactions, *Langmuir*, 2017, **33**, 6372–6381.
- 23 X. Xiong, Y. Tang, C. Xu, Y. Huang, Y. Wang, L. Fu, C. Lin, D. Zhou and Y. Lin, High Carbonization Temperature to Trigger Enzyme Mimicking Activities of Silk-Derived Nanosheets, *Small*, 2020, **16**, 2004129.
- 24 Y. Yang, M. Chen, B. Wang, P. Wang, Y. Liu, Y. Zhao, K. Li, G. Song, X. B. Zhang and W. Tan, NIR-II Driven Plasmon-Enhanced Catalysis for a Timely Supply of Oxygen to Overcome Hypoxia-Induced Radiotherapy Tolerance, *Angew. Chem., Int. Ed.*, 2019, **58**, 15069–15075.
- 25 Z. Moosavi-Movahedi, E. S. Kalejahi, M. Nourisefat, P. Maghami, N. Poursasan and A. A. Moosavi-Movahedi, Mixed SDS-Hemin-Imidazole at low ionic strength being efficient peroxidase-like as a nanozyme, *Colloids Surf., A*, 2017, **522**, 233–241.
- 26 Y. G. Zhou, Y. Kang and J. Huang, Fluidized Electrocatalysis, *CCS Chem.*, 2020, **2**, 31–41.
- 27 J. Fan, J. Lu, Z. Sha, W. Zuo, X. Fei and M. Zhu, Conformally anchoring nanocatalyst onto quartz fibers enables versatile microreactor platforms for continuous-flow catalysis, *Sci. China: Chem.*, 2021, **64**, 1596–1604.
- 28 V. Srivastava, P. P. Singh, S. Sinha, P. K. Singh and D. Kumar, Continuous-Flow Photochemistry: The Synthesis of Marketed Pharmaceutical Compounds, *ChemistrySelect*, 2024, **9**, e202405020.
- 29 K. Vijaya Bhaskar, M. Rashed, K. Subrahmanya Bhat, J. Lee, K. H. Kim and K. Buruga, A continuous flow microreactor as a practical tool for the synthesis of active pharmaceutical ingredients, *Process Saf. Environ. Prot.*, 2024, **192**, 437–449.
- 30 Y. Liu, M. Shang, S. Liu, X. Xue, Z. Zhong, Q. Niu and Y. Su, Continuous-flow synthesis of di-(2-ethylhexyl) peroxydicarbonate in a packed-bed microreactor: Process optimization and kinetic modeling, *Chem. Eng. Sci.*, 2024, **299**, 120499.
- 31 S. Wu, C. Chen, R. Shi, C. Zhou and P. Wang, A multistep continuous microreactor platform for rapid preparation of CoS@NiS nanosheets with efficient electrocatalytic hydrogen evolution, *Fuel*, 2024, **371**, 132048.
- 32 P. A. Peñaranda, M. J. Noguera, S. L. Florez, J. Husserl, N. Ornelas-Soto, J. C. Cruz and J. F. Osma, Treatment of Wastewater, Phenols and Dyes Using Novel Magnetic Torus Microreactors and Laccase



- Immobilized on Magnetite Nanoparticles, *Nanomaterials*, 2022, **12**, 1688.
- 33 Q. Shang, M. Guo, J. Zhang, M. Liu, K. Lin, H. Li, G. Cui, X. Shi and B. Tang, Gas-liquid-solid triphasic continuous flow microreactor for improving homogeneous distribution of solid composites in heterogeneous photocatalytic degradation progress, *Sep. Purif. Technol.*, 2024, **348**, 127698.
 - 34 P. Zhang, D. Sun, A. Cho, S. Weon, S. Lee, J. Lee, J. W. Han, D. P. Kim and W. Choi, Modified carbon nitride nanozyme as bifunctional glucose oxidase-peroxidase for metal-free bioinspired cascade photocatalysis, *Nat. Commun.*, 2019, **10**, 940.
 - 35 Q. Zhou, H. Yang, X. Chen, Y. Xu, D. Han, S. Zhou, S. Liu, Y. Shen and Y. Zhang, Cascaded Nanozyme System with High Reaction Selectivity by Substrate Screening and Channeling in a Microfluidic Device, *Angew. Chem., Int. Ed.*, 2022, **61**, e202112453.
 - 36 Y. T. Wang, M. Wang, K. Z. Yang and Z. L. Zhang, A corresponding V-target lattice structure to enhance selection pressure for aptamer selection, *Sens. Diagn.*, 2023, **2**, 418–426.
 - 37 H. Zhang, S. Yao, X. Song, K. Xu, J. Wang, J. Li, C. Zhao and M. Jin, One-step colorimetric detection of *Staphylococcus aureus* based on target-induced shielding against the peroxidase mimicking activity of aptamer-functionalized gold-coated iron oxide nanocomposites, *Talanta*, 2021, **232**, 122448.
 - 38 N. Duan, S. Wu, X. Chen, Y. Huang, Y. Xia, X. Ma and Z. Wang, Selection and Characterization of Aptamers against *Salmonella typhimurium* Using Whole-Bacterium Systemic Evolution of Ligands by Exponential Enrichment (SELEX), *J. Agric. Food Chem.*, 2013, **61**, 3229–3234.
 - 39 A. G. Bozkurt, G. G. Buyukgoz, M. Soforoglu, U. Tamer, Z. Suludere and I. H. Boyaci, Alkaline phosphatase labeled SERS active sandwich immunoassay for detection of *Escherichia coli*, *Spectrochim. Acta, Part A*, 2018, **194**, 8–13.
 - 40 X. Zhang, Q. Yang, Y. Lang, X. Jiang and P. Wu, The Rationale of 3,3',5,5'-Tetramethylbenzidine (TMB) as the Chromogenic Substrate in Colorimetric Analysis, *Anal. Chem.*, 2020, **92**, 12400–12406.

